Materials & Design 220 (2022) 110886

Contents lists available at ScienceDirect

Materials & Design

journal homepage: www.elsevier.com/locate/matdes

Tuning the microstructure, martensitic transformation and superelastic properties of EBF^3-fabricated NiTi shape memory alloy using interlayer remelting

Binqiang Li [a], Liang Wang [a,*], Binbin Wang [a], Donghai Li [a], J.P. Oliveira [b,d], Ran Cui [a], Jianxin Yu [c], Liangshun Luo [a], Ruirun Chen [a], Yanqing Su [a,*], Jingjie Guo [a], Hengzhi Fu [a]

[a] National Key Laboratory for Precision Hot Processing of Metals, School of Materials Science and Engineering, Harbin Institute of Technology, Harbin 150001, China
[b] UNIDEMI, Department of Mechanical and Industrial Engineering, NOVA School of Science and Technology, Universidade NOVA de Lisboa, 2829-516 Caparica, Portugal
[c] Center of Analysis, Measurement and Computing, Harbin Institute of Technology, Harbin, 150001, China
[d] CENIMAT/I3N, Department of Materials Science, NOVA School of Science and Technology, Universidade NOVA de Lisboa, 2829-516 Caparica, Portugal

HIGHLIGHTS

- Interlayer remelting strategies can regulate the microstructure evolution, martensitic transformation, and superelasticity of EBF^3-fabricated NiTi SMAs.
- A one-step reversible transformation (B2 ↔ B19′) occurred upon heating/cooling.
- The critical stress (σ^{Ms}) has a strong dependence on the martensitic transformation behavior.
- The broadening and stabilization of martensite is the key factor for the deterioration of the superelastic response.

GRAPHICAL ABSTRACT

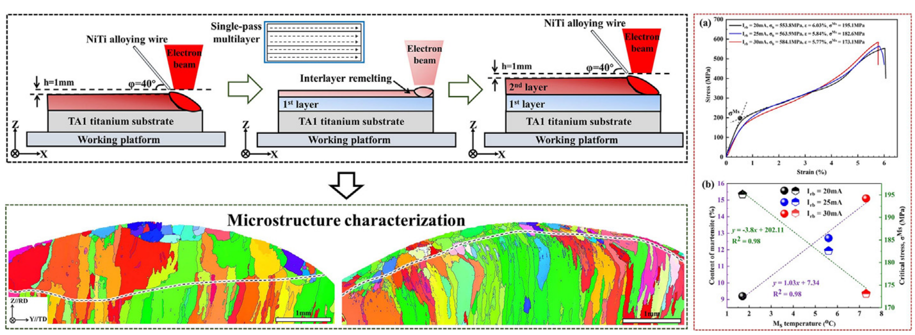

ARTICLE INFO

Article history:
Received 21 April 2022
Revised 8 June 2022
Accepted 22 June 2022
Available online 26 June 2022

Keywords:
NiTi deposits
Interlayer remelting
Martensitic transformation
Superelasticity
Plastic deformation

ABSTRACT

In this work, different interlayer remelting strategies are applied to regulate the microstructure evolution, martensitic transformation, and superelastic features of NiTi shape memory alloys prepared using the EBF^3 additive manufacturing technique. The NiTi deposits prepared under different remelting beam currents are all composed of the B2 austenite, residual B19′ martensite, and submicron-scale $Ti_4Ni_2O_x$ precipitates, and exhibit a one-step phase transformation (B2 ↔ B19′). Meanwhile, the crystallographic orientation, grain boundaries, and residual strain of these alloys present a distinct variation with the application of different remelting beam currents. During mechanical testing, the critical stress (σ^{Ms}) of the EBF^3-fabricated NiTi alloys was seen to possess a significant dependence on the martensitic transformation behavior, namely with the amount of B19′ martensite and the corresponding M_s. However, the broadening and stabilization of lamellar martensite created by dislocation pile-ups and plastic deformation in the cyclic loading–unloading procedure is the key reason for the deterioration of the superelastic response of the NiTi deposits. This work confirms that the mechanical and functional performances of NiTi alloys produced via EBF^3-technique can be modified upon the application of proper interlayer remelting strategies, which can be extrapolated to the directed energy deposition of shape memory alloys or other metal components.

* Corresponding authors.
E-mail addresses: wliang1227@hit.edu.cn (L. Wang), suyq@hit.edu.cn (Y. Su).

https://doi.org/10.1016/j.matdes.2022.110886
0264-1275/

1. Introduction

Additive manufacturing (AM) of NiTi shape memory alloys (SMAs) has been attracting consideration recently owing to the possibility to combine the functional properties of these materials, the shape memory effect (SME) and superelasticity (SE), coupled with the increased freedom of design enabled by AM [1–4]. In terms of current development, directed energy deposition (DED) of NiTi SMAs is a prospective alternative to enable the fabrication of large functional components based on this AM technology [5,6]. Compared to powder-based laser deposition, wire-based vacuum additive manufacturing technique, also named electron beam freeform fabrication (EBF^3), has better suitability for the rapid production of large-size NiTi parts, which is attributed to its efficient fusion penetration, vacuum environment, and high deposition efficiency [7–9].

Dutkiewicz et al. [7] were the first to manufacture a Ni-rich NiTi deposit with a size of 5 × 10 × 45 mm using the EBF^3-technique using a set of process parameters, where the accelerating voltage, beam current, feeding angle, feeding speed, and travel speed were 60 kV, 15 mA, 30°, 1 m/min, and 2 m/min, respectively. They found the martensite start temperature (M_s) of the as-deposited NiTi specimen was 2.2 °C, and a subsequent aging treatment (500 °C for 2 h) not only created R-phase but also shifted the martensitic transformation temperatures (MTTs) to higher values. Immediately after, the epitaxial growth mechanism, phase transformation, and superelastic response of these NiTi alloys were investigated by the same team in [10]. Similarly, the influence of the number of deposition layers on porosity, microstructure, and martensitic transformation was studied by Guimarães et al. [8]. Their results indicated the presence of a columnar-like grain structure and a one-step reversible transformation (B2 ↔ B19′) in all as-deposited NiTi alloy. Besides, the work of Pu et al. [9] demonstrated that the MTTs and superelasticity of wire-based vacuum AM-processed NiTi alloys depend on the height of deposit, but proper heat treatments can promote uniformity of phase transformation and superelasticity throughout the part. Our previous research also confirmed that there are obvious differences along the building and deposition directions in terms of microstructural features, martensitic transformation, tensile properties, and superelasticity of EBF^3-fabricated NiTi part [11]. Therefore, the elimination of such microstructure variation along the height of the fabricated and the improvement of mechanical and functional performances of the component through process optimization is an urgent requirement for the production of high performing NiTi SMAs via EBF^3-technique.

The interlayer remelting strategy is to apply an additional low-power energy beam, to the upper surface of the current deposited layer to achieve local remelting. This method has been frequently employed during AM to mitigate potential process-related defects, control the grain size, alter the crystallographic orientation, and enhance the mechanical properties [13–15]. Zhan et al. [16] proposed that interlayer remelting is also applicable to the selective laser melting (SLM) of NiTi SMAs, which can increase the part density, raise MTTs, and improver the ultimate tensile strength (UTS) and elongation (EL) of the fabricated components. Similarly, the interlayer remelting strategy was applied to the powder-based laser-directed energy deposition technique for NiTi SMAs by Gao et al. [17]. They concluded through numerical simulations and experimental characterization that interlayer remelting by low-power laser beams can promote in-situ heat treatment, which can produce transient solution treatment, stabilizing phase transformation, and reduce the precipitates content. However, the use of interlayer remelting during with EBF^3-fabricated NiTi alloy has not been reported so far. Therefore, the effect of beam currents of interlayer remelting on the microstructural modulation, martensitic phase transformation, mechanical performance, and superelastic deformation of NiTi alloy fabricated using EBF^3-technique are investigated in detail in this work. We aim to shed an improved understanding on the relationship between the interlayer remelting strategy and the mechanical and functional behavior, which can facilitate the process of the rapid manufacturing of high-quality NiTi SMAs components by EBF^3.

2. Preparation and investigation process

2.1. Fabrication process

The single wall multilayer NiTi parts were manufactured on EBF^3 equipment (ZcompleX3, DMAMS, Xi'an, China) using an interlayer remelting process under different beam currents. A high-energy electron beam is formed by exciting a direct-heat tungsten filament. Specifically, the cold-drawn Ti-50.7 %Ni (unless otherwise illustrated, all percentages refer to atomic percentages) wire with a diameter of 1.6 mm was deposited on a TA1 plate by feeding it into the molten pool created by an electron beam. The corresponding process conditions, included vacuum level, oscillation mode, accelerating voltage, beam current, travel speed, and feeding speed set to 7 × 10^{-2} Pa, liquid bridge transition, 60 kV, 45 mA, 600 mm/min, and 3 m/min, respectively. Detailed information on the raw materials adopted for this study can be obtained in literature [11] and [12], including chemical composition and microstructure. Next, interlayer remelting of the previously deposited NiTi layer was performed under different beam currents (I_{rb}: 20 mA, 25 mA, and 30 mA) at a travel speed of 600 mm/min. Afterward, the solidified deposition layer dropped by 1 mm, and a new NiTi layer was deposited by continuously feeding the wire according to the process parameters used in the first step. The remelting was again employed and the process continued until achieving a desired part heigh. A schematic representation of the selected process-unit is detailed in Fig. 1(a). Finally, the as-deposited NiTi wall with an approximate size of 80 mm × (7.4 ~ 9.2) mm × 45 mm was obtained.

2.2. Characterization and analysis

As represented in Fig. 1(b), all specimens were extracted along the building direction (BD) and their Y-Z sections were observed and tested. In detail, we measured the average relative density of these NiTi alloys using the Archimedes method, considering a reference density of 6.45 g/cm^3, with three blocks of size 6 × 6 × 6 mm. Inductively coupled plasma optical emission spectroscopy (ICP-OES, iCAP 7400, Thermo, Germany) was employed to identify the chemical composition of the NiTi deposits. The phase constitution was analyzed using X-ray diffraction (XRD, Empyrean, Panalytical, Netherlands) with Cu-Kα radiation at room temperature, and Rietveld refinement was applied to quantify the volume fraction of B2 austenite and B19′ martensite. Scanning electron microscopy (SEM, SUPRA55, ZEISS, Germany) equipped with energy-dispersive spectroscopy (EDS) and an electron backscattered diffraction (EBSD) detector, electron probe microanalysis (EPMA, JXA-8230, JEOL, Japan) allocated with wavelength dispersive spectrometry (WDS), and transmission electron microscope (TEM, Talos F200X, FEI, USA) were used to interpret the microstructure evolution, crystallographic orientation, and existing precipitates. Specifically, the EPMA samples are prepared using standard mechanical grinding and polishing methods until a mirror-like surface is obtained. The samples for SEM were polished mechanically and then etched in solution composed of 1 ml HF, 4 ml HNO_3, and 5 ml H_2O for 15 s. Similarly, the specimens for EBSD were polished mechanically, and then electrolytic polishing

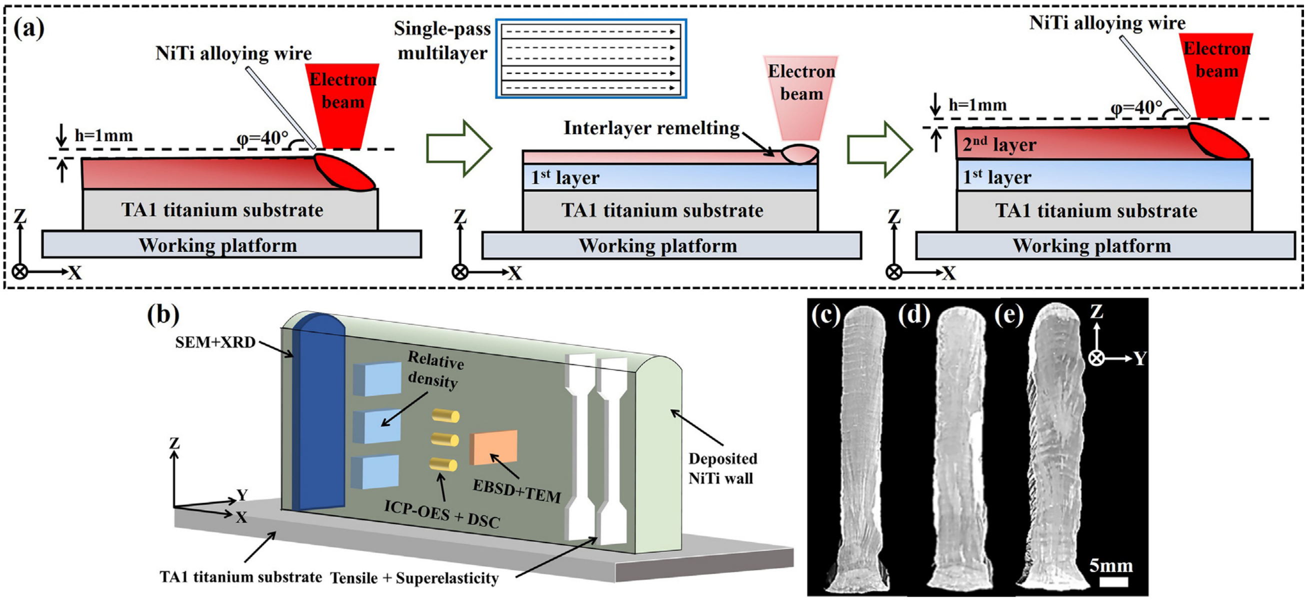

Fig. 1. EBF³-fabrication process using interlayer remelting and its deposit information: (a) schematic representation of the deposition procedure; (b) visualization of sample extraction locations; (c), (d), and (e) are the macroscopic morphology of the Y-Z section of the deposits.

was used to remove the mechanically affected surface. The electrolytic polishing instrument was performed at 20 V in a solution of 60 vol% methanol, 34 vol% Nbutanol, and 6 vol % perchloric acid cooled to −10 °C, where the current and time were maintained at 0.9–1.2 A and 2 min, respectively. Subsequently, EBSD data were acquired at an accelerating voltage of 20 kV and with a step size of 1 μm, and the raw data were post-processed with AZtecCrystal 2.1 software. Moreover, a disc with a diameter of 3 mm and a thickness of 0.3 mm was mechanically ground to a thickness of less than 50 μm, and then the center of the sample was perforated under a GATAN695 Ar ion thinning instrument at an inclination angle of 8°, and then the inclination angle was adjusted to 6° and 3° by gentle grinding, which resulted in an electron-transparent film for TEM observation. Following the ASTM F2004-05 standard, differential scanning calorimetry (DSC, STA449F3, Netzsch, Germany) was employed to determine the martensitic transformation process between −70 °C and 150 °C at a heating/cooling rate of 10 °C/min in a nitrogen atmosphere.

To evaluate the mechanical properties of these NiTi alloys, the samples (gauge length is 20 mm, width is 3 mm, and thickness is 1 mm) were deformed using an electronic universal testing machine (AGXplus, Shimadzu, Japan) at a strain rate of 8×10^{-5} s^{-1} at room temperature. The critical stress for the stress induced martensite transformation (σ^{Ms}), ultimate tensile strength (UTS, σ_b), and elongation (EL, ε) were obtained from the stress–strain curves. The corresponding fracture morphology was also observed by employing SEM to explore their fracture mechanism. Moreover, 10 load-unload cycles at three different maximum strains (3%, 4%, and 5%) were completed at a strain rate of 8×10^{-5} s^{-1} under tensile loading conditions. In detail, the samples were first loaded to the selected maximum strain, i.e., 3%, 4%, or 5%, and unloaded to a stress-free state. Next, the samples were again loaded to a predetermined maximum strain and then unloaded to stress-free. The process continued until the 10 tensile cycles were completed. During this process, the superelastic recovery ratio was recorded to investigate the superelastic deformation phenomenon. After cyclic loading, samples were analyzed by TEM to detail the connection between the superelastic response and plastic deformation of as-deposited NiTi alloys using the EBF³-technique under different remelting beam currents.

3. Results

3.1. Deposition level, phase constitution, and microstructure

The appearance of the Y-Z section of these NiTi deposits under various remelting beam currents is displayed in Fig. 1(c) to Fig. 1(e). It can be clearly seen that the fabricated specimens present a good forming quality. Specifically, both the average width and relative density of the NiTi alloys grow with the increase of the remelting beam currents, as detailed in Table 1. Actually, the width of the NiTi deposit does not depend entirely on the diameter of the wire, rather there is a coupling effect between the wire diameter and the selected processing parameters. Compared with the deposit without remelting, the average relative density of all interlayer remelted specimens was improved (99.68%, 99.79% and 99.83% vs 99.62%). However, the interlayer remelting promotes an increased tendency for preferential volatilization of Ni in the EBF³-fabricated NiTi deposit. Thus, the Ni content is negatively correlated with the remelting beam current. This is mainly due to the fact that larger beam current or energy density promote an increasing peak temperature in the melt pool, which in term will promote more significantly the preferential evaporation of Ni over Ti [11,12,18–20].

Fig. 2 details the representative XRD patterns and Rietveld refinement results with remelting beam currents of 20, 25 and 30 mA. Similar to the XRD results of the un-remelted sample presented in Fig. S1(a) of *Supplementary Materials*, all the NiTi deposits contain B2 austenite and B19′ martensite phases at room temperature, as shown in Fig. 2(a). Meanwhile, the content of the B19′ martensite in the interlayer remelted NiTi alloys gradually grows with the increase of the remelting beam current, and their mass percentage is higher (5.6%) than that of the un-remelted samples. Considering the preferential evaporation of Ni with increasing beam current, this increase in the volume fraction of martensite was, therefore, expected. The mass percentage of martensite reaches its highest value of 15.1% when the remelting beam current is 30 mA, as exhibited in Fig. 2(c). However, the EBF³-fabricated NiTi alloy is still dominated by austenite with a fraction of 84.9% at ambient temperature. The specific correlations will be discussed in detail in *Section 3.3*.

Table 1
Chemical composition, dimensions, and relative density of as-deposited NiTi alloys under different remelting beam currents.

I_{rb} (mA)	Composition (at. %)				Average width (mm)	Density (g/cm^3)			Average relative density (%)
	Ni	Ti	Other	Ni/Ti					
0 [a]	50.41	49.52	0.072	1.018	7.4	6.425	6.435	6.426	99.62
20	50.32	49.61	0.071	1.014	7.4	6.423	6.431	6.435	99.68
25	50.28	49.65	0.073	1.013	8.3	6.431	6.446	6.432	99.79
30	50.17	49.76	0.074	1.008	9.2	6.437	6.441	6.439	99.83

[a] I_{rb} equals 0 for the deposit without interlayer remelting.

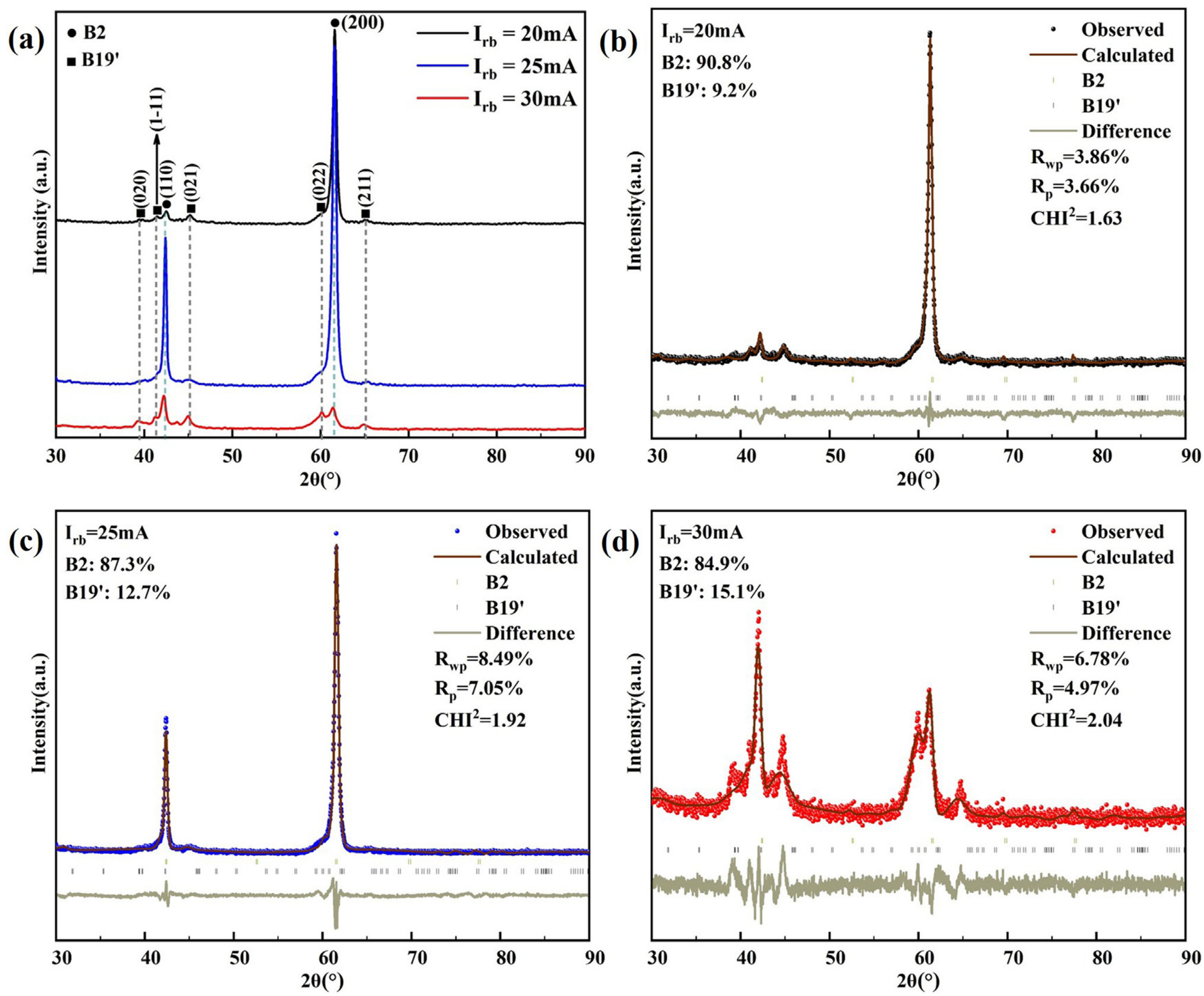

Fig. 2. Representative XRD patterns of as-deposited NiTi alloys under different remelting beam currents: (a) full patterns; (b), (c), and (d) correspond to the Rietveld refinement results with remelting beam currents of 20, 25 and 30 mA, respectively.

Fig. 3 details the microstructure characterization of the Y-Z section of these NiTi alloys under various remelting beam currents. All the NiTi deposits have similar microstructure, and they consist of epitaxially grown NiTi columnar grains and submicron-scale precipitates. Meanwhile, the spacing between the columnar grains widens with increasing remelting beam currents, as shown in Fig. 3(a) to Fig. 3(c), which is attributed to a higher interlayer remelting beam current promoting a homogenization of the temperature gradient and reducing the material cooling rate. The EPMA results shown in Fig. 3(d) reveal that the precipitates in the EBF^3-fabricated NiTi deposits are Ti-rich, Ni-lean and with trace amounts of O. Combined with our previous investigations [11,12], it can be inferred that these precipitates are $Ti_4Ni_2O_x$, which are easily formed in NiTi SMAs owing to the high affinity of the material with oxygen at high temperatures. However, the area fraction of $Ti_4Ni_2O_x$ precipitates decreases from 2.47 to 1.56% with the increase of the remelting beam current from 20 to 30 mA. This is mainly related to the larger remelting beam current as it facilitates the diffusion of solute elements into the matrix and reduces the solute segregation at the grain boundaries, thus diminishing the content of $Ti_4Ni_2O_x$ located in the interdendritic space. The presence of the $Ti_4Ni_2O_x$ precipitates have an effect on the mechanical

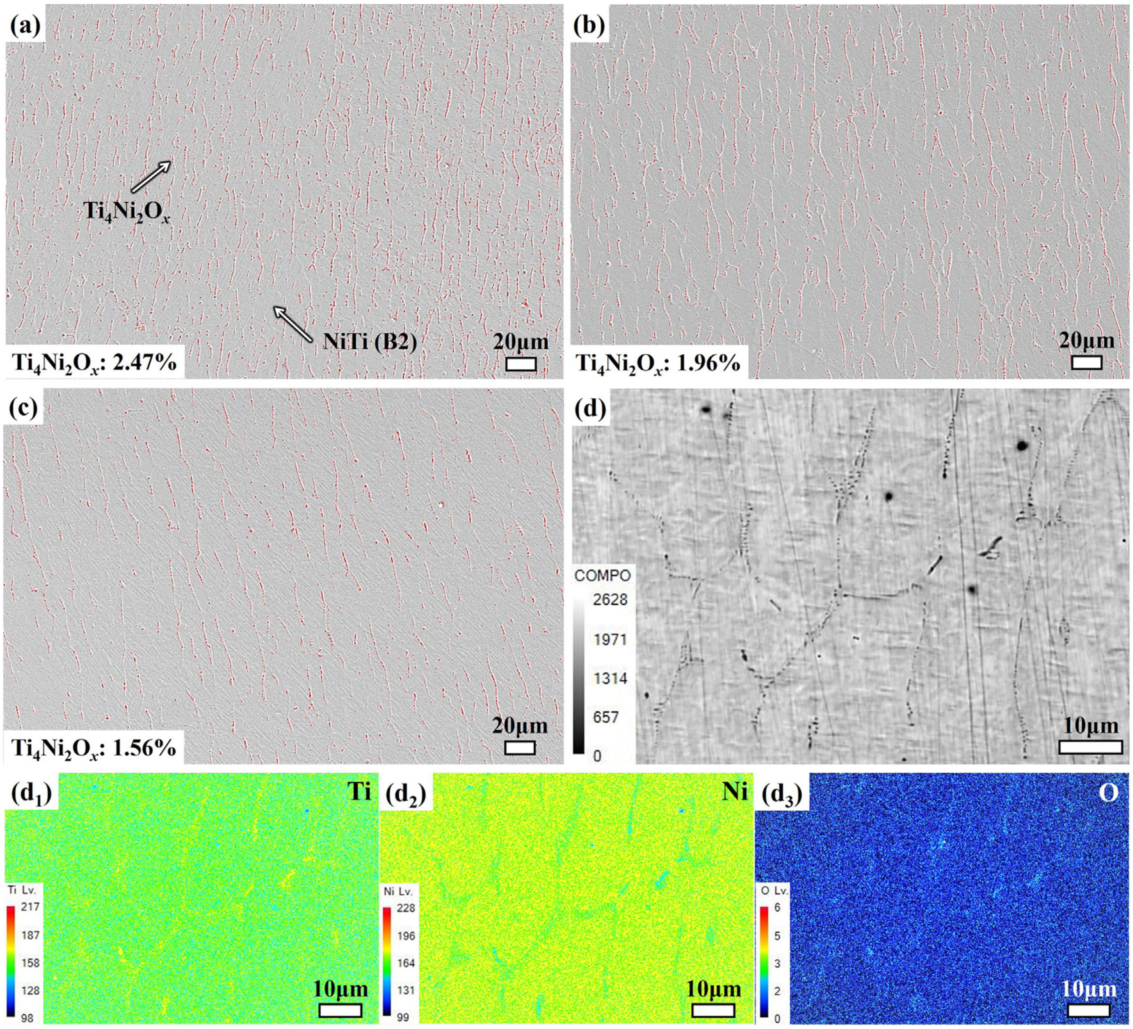

Fig. 3. Microstructure characterization of the Y-Z section of the as-deposited NiTi alloys under various remelting beam currents: (a) 20 mA; (b) 25 mA; (c) 30 mA; (d) backscattered image of NiTi deposit with a remelting beam current of 20 mA; (d_1), (d_2), and (d_3) are the corresponding distribution maps of Ti, Ni, and O, respectively.

properties and superelastic response of the as-deposited NiTi alloys, which will be described in detail in *Sections 3.4 and 4.3*, respectively.

TEM analysis of the as-deposited NiTi alloy with the remelting beam current of 20 mA was conducted to further complement the microstructure characterization as detailed in Fig. 4. It can be confirmed in Fig. 4(a) to Fig. 4(c) that the NiTi deposit consists mainly of the B2 austenite, and evidence of lamellar B19′ martensite is also presented. The selected area electron diffraction (SAED) patterns in Fig. 4(c) indicates that the martensite belongs to the (100) compound twins. Meanwhile, the high angle annular dark-field (HAADF) image and the corresponding elemental distribution show that the submicron-scale precipitates are $Ti_4Ni_2O_x$, which is consistent with the results of Fig. 3 and that of our previous study [11,12].

3.2. Texture and grain characteristic of the B2 austenite phase

Based on the results detailed in Fig. 3 and Fig. 4, EBSD analysis of the austenitic phase was used to analyze the orientation, texture, and grain characteristics of the as-deposited NiTi alloys under the various remelting beam currents. The coordinate system, as shown in Fig. 5(j), considers the relationship between the spatial location of the deposit and the sample location at the time of EBSD data acquisition. All orientation maps are the result of projection along the normal direction (ND) on the sample referential. This referential and projection relationship are used throughout the text when referring to EBSD data if not otherwise specified. As displayed in Fig. 5(a), Fig. 5(b), and Fig. 5(c), the epitaxial columnar crystals grow along the building direction. The grain boundaries of NiTi alloy are almost all low-angle grain boundaries (LAGBs, 2°∼15°) when the remelting beam current is 20 mA. However, the content of LAGBs gradually decreased from 0.99 to 0.86 with the increase of remelting beam current, as exhibited in Fig. 5(d) to Fig. 5(f). This is mainly because the small remelting beam current leads to a more pronounced temperature gradient, which promotes the continuous epitaxial grow along the building direction with LAGBs. The larger remelting beam current moderates the interlayer deviation of the temperature gradient and promotes the formation of more grain boundaries. Similarly, the increase in remelting beam currents also resulted in a change in the texture of the B2 austenite phase. It can be observed from the {100} pole figure (PF) presented in Fig. 5(g) to Fig. 5(i) that the texture type of the B2 austenite phase transformed from a Cube texture {001} ⟨100⟩ into a Goss texture {110} ⟨001⟩ with the increase in the remelting beam current.

To further explore the effect of remelting beam currents on the crystallographic orientation of the B2 austenite, the texture recon-

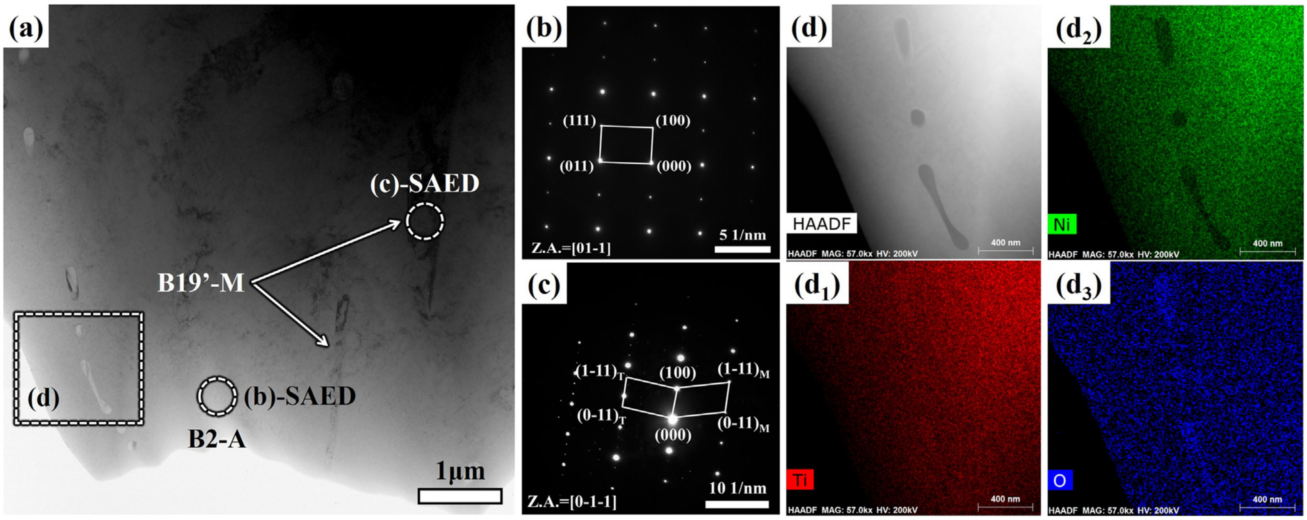

Fig. 4. TEM imaging of the NiTi alloy fabricated with a remelting beam current of 20 mA: (a) overall bright-field image; (b) SAED of B2 austenite; (c) SAED of B19′ martensite; (d) HAADF image of precipitates; (d_1) Ti map; (d_2) Ni map; (d_3) O map.

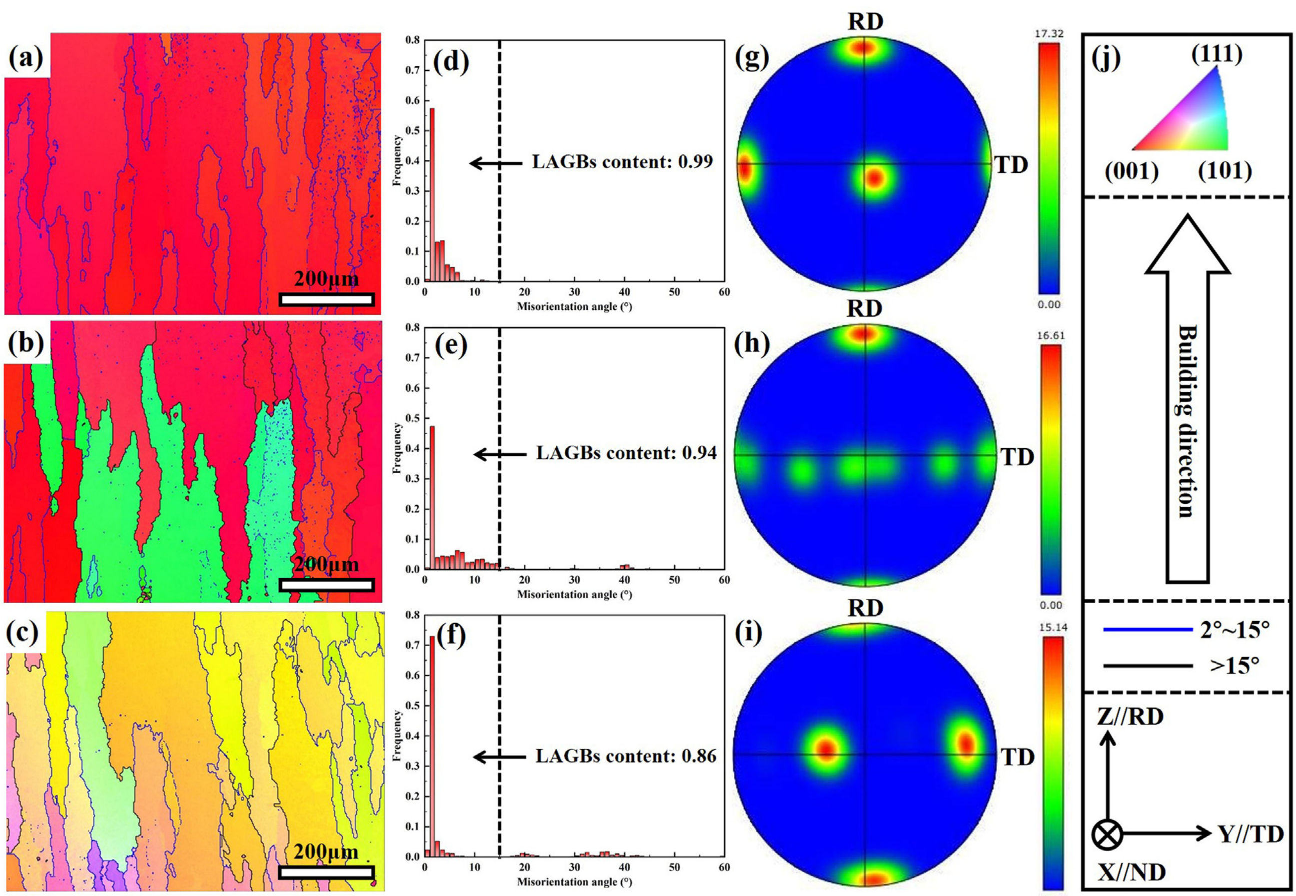

Fig. 5. EBSD analysis of the as-deposited NiTi alloys under various remelting beam currents: (a), (b), and (c) are the orientation profiles and grain boundaries for remelting beam currents of 20, 25 and 30 mA, respectively; (d), (e), and (f) are the misorientation for remelting beam currents of 20, 25 and 30 mA, respectively; (g), (h), and (i) are the {100} pole figure for remelting beam currents of 20, 25 and 30 mA, respectively; (j) related legends, such as color distribution of orientation, building direction, type of grain boundaries, and reference coordinate system.

struction of the EBF^3-fabricated NiTi alloys was performed. As depicted in Fig. 6(a) to Fig. 6(c), the red and blue colors of the linear gradient represent the Cube {001} ⟨100⟩ and Goss {110} ⟨001⟩ textures, respectively. The results indicate that the Cube {001} ⟨100⟩ texture completely dominates the deposit fabricated with a remelting beam current of 20 mA. However, the content of Goss {110} ⟨001⟩ texture increases up to 33.4% when the remelting beam current is 25 mA. The crystallographic orientation

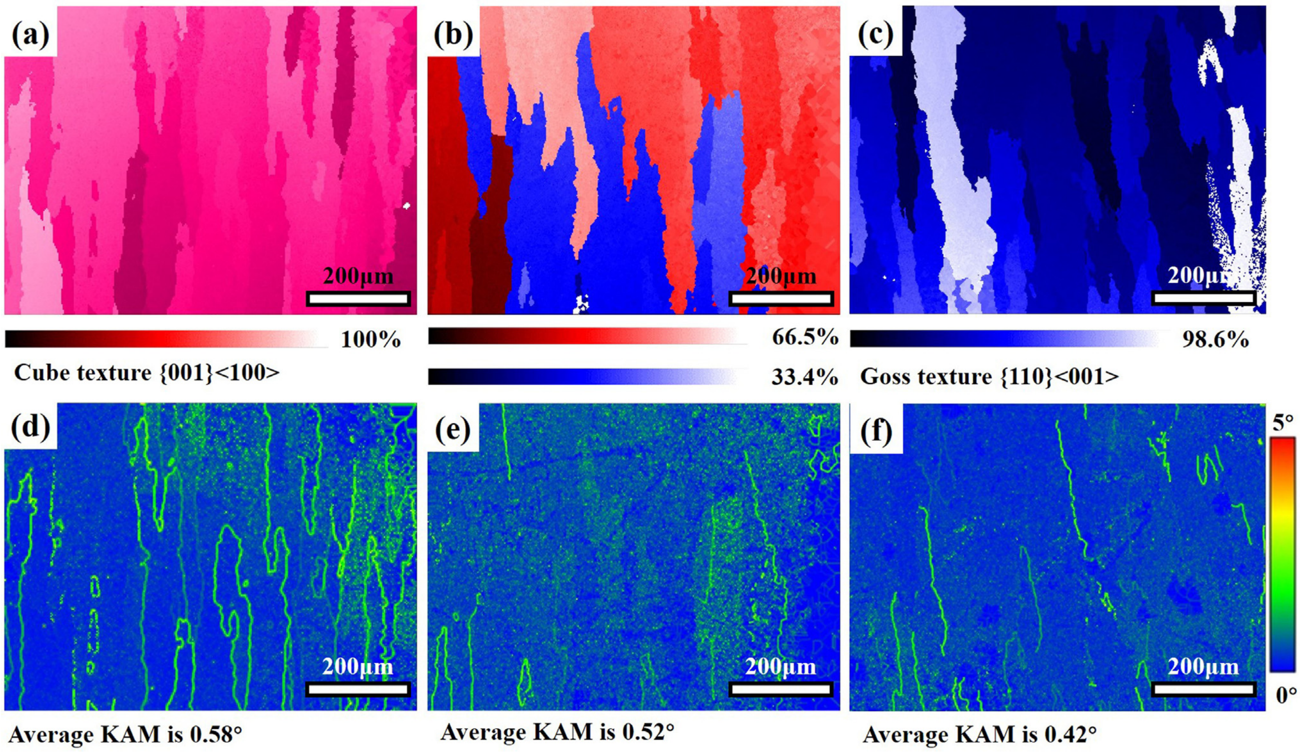

Fig. 6. Crystallographic texture and KAM maps of the as-deposited NiTi alloys under various remelting beam currents: (a), (b), and (c) are the distribution and content of texture for remelting beam currents of 20, 25 and 30 mA, respectively; (d), (e), and (f) are the KAM maps for remelting beam currents of 20, 25 and 30 mA, respectively.

is almost transformed into {1 1 0} ⟨0 0 1⟩ with the remelting beam current is increased to 30 mA, as displayed in Fig. 6(c), and a small amount of unidentified texture (1.4 %) was observed and this is due to a minor deflection of the actual orientation position compared to the standard Goss texture. Moreover, the kernel average misorientation (KAM) map is a common and effective analytical method in EBSD data post-processing to calculate the local mismatch angle. Thus, we obtained the corresponding KAM maps to qualitatively reflect the relationship between remelting beam currents and residual strain during the EBF^3-fabrication process. It can be found from Fig. 6(d) to Fig. 6(f) that all the NiTi alloys prepared by EBF^3-technique possess a large KAM at the LAGBs. However, the value of average KAM decreases gradually from 0.58 to 0.42° with increasing remelting beam current. This indicates that an appropriate interlayer remelting strategy can regulate the residual strain in the NiTi deposits with the effects of in-situ heat treatment, which is prevalent in additive manufacturing of metals [21–23]. The variation of residual strain has an influence on the phase transformation behavior of the as-deposited NiTi alloys, such as transformation temperature or transformation route. The specific relationships will be further evaluated in *Section 3.3*.

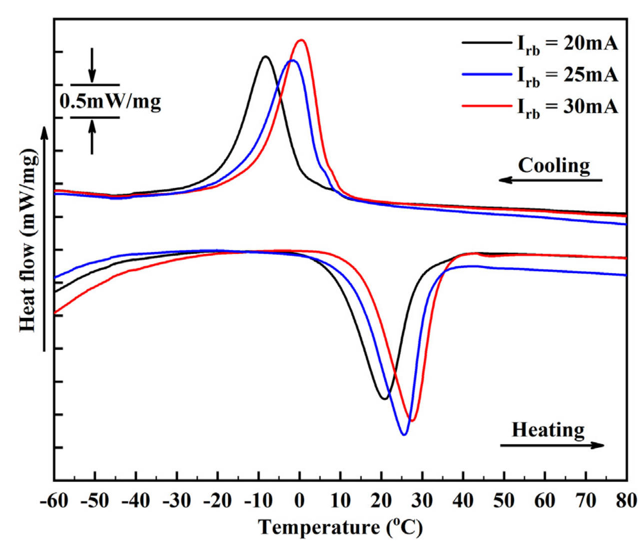

Fig. 7. DSC curves of the as-deposited NiTi alloys under the various remelting beam currents.

3.3. Martensitic transformation

Fig. 7 details the DSC curves of the as-deposited NiTi alloys under various remelting beam currents. Similar to the DSC results of the un-remelted sample presented in Fig. S1(b) of *Supplementary Materials*, a one-step phase transformation between B2 austenite and B19′ martensite is found for all NiTi deposits in both heating and cooling. Meanwhile, the specific transformation temperatures including M_f, M_p, M_s, A_s, A_p, and A_f were determined by the standard tangent method and these temperatures are listed in Table 2. It can be identified that the value of M_s increases with the increase of remelting beam current, which is closely related to the concentration of the Ni and residual stress in the NiTi alloy. Specifically, the value of M_s in the un-remelted NiTi deposit is −4.9 °C, which is significantly lower than the M_s of the interlayer remelted specimens. As generally known, a 0.1 at. % decrease in the content of Ni element will result in an increase of M_s temperature of about 10 °C in NiTi SMAs [24,25]. Similarly, Feng et al. [26] and Guo et al. [27] have demonstrated that Ni volatilization is the main factor promoting the increase of transformation temperatures in SLM-processed NiTi alloys, followed by the effect of precipitates and residual stresses. According to the results detailed in Table 1, the Ni content reduced from 50.41 to 50.17 at. % when the remelting

Table 2
Specific transformation temperatures of the as-deposited NiTi alloys under various remelting beam currents.

I_{rb} (mA)	Transformation temperature [a] (°C)						ΔT (°C)
	M_f	M_p	M_s	A_s	A_p	A_f	
0 [b]	−26.4	−11.8	−4.9	4.2	16.8	29.7	32.6
20	−18.6	−8.3	1.7	8.6	20.8	29.8	27.7
25	−15.7	−1.5	5.6	12.8	25.6	32.4	27.7
30	−11.1	0.8	7.3	15.3	27.5	34.5	26.8

[a] The definition of MTTs remains in agreement with our earlier study [11].
[b] I_{rb} equals 0 for the deposit without interlayer remelting.

beam current increased from 0 to 30 mA. Therefore, the M_s and A_f of the as-deposited NiTi alloys raised with the increase of the remelting beam currents, which further stabilized more martensite at ambient temperature in the as-built parts, as shown in Fig. 2. In addition, the thermal hysteresis (ΔT) of the phase transformation was calculated by $(A_s + (A_f - A_s)/2) - (M_f + (M_s - M_f)/2)$ according to [28]. The thermal hysteresis, ΔT, of these NiTi alloys under various remelting beam currents is kept at nearly 27 °C. Compared with the results of the un-remelted deposits, the preservation of the thermal hysteresis is attributed to the homogeneity of microstructure induced by the interlayer remelting [27].

3.4. Mechanical behavior and superelastic response

Representative tensile stress–strain curves of the as-deposited NiTi alloys under various remelting beam currents are displayed in Fig. 8. It can be obviously seen that the σ_b and ε are positively and negatively correlated with the enhancement of remelting beam currents, respectively, where the σ_b increase from 554 to 584 MPa and ε decreases from 6.03 to 5.77%. Meanwhile, the typical transformation plateaus are present in all EBF^3-fabricated NiTi deposits. According to the tangent rule, the critical stresses for the stress induced martensitic transformation (σ^{Ms}) during the tensile loading was determined. The values of σ^{Ms} reduce from 195 to 173 MPa with the increase of the remelting beam current from 20 to 30 mA. Actually, the level of σ^{Ms} in NiTi SMAs is strongly dependent on internal and external parameters, such as chemical composition, transformation temperatures, content of residual martensite, and crystallographic orientation [29,30]. In the current work, the connection between remelting beam currents and σ^{Ms} will be comprehensively detailed in *Section 4.2*. Compared with

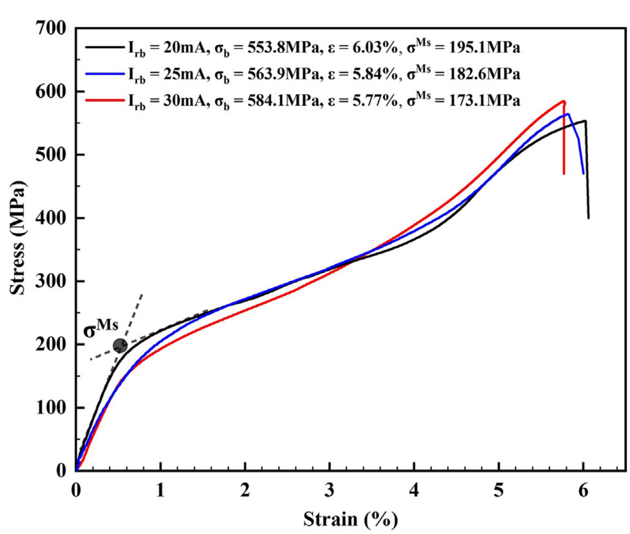

Fig. 8. Representative the tensile stress–strain curves of the as-deposited NiTi alloys under different remelting beam currents.

the tensile properties of the un-remelted NiTi deposit exhibited in Fig. S1(c) of *Supplementary Materials*, moreover, the ε of all interlayer remelted deposits was higher than that of the un-remelted samples by 4.61%. For additively manufactured NiTi shape memory alloys, it is of great interest to obtain good elongation in the building direction, since the choice of its superelasticity strain range is closely related to the magnitude of the elongation. Therefore, the increase in elongation justifies the introduction of interlayer remelting during the EBF^3-fabrication process.

To explore the superelasticity of as-deposited NiTi alloys with pre-strain, the superelastic response of these NiTi deposits fabricated under different remelting beam currents during cyclic loading–unloading testing was investigated. The results of remelting beam current of 20 mA, as depicted in Fig. 9(a) to Fig. 9(c), indicate that the recovery ratio of reversible strain (ε_r) in the first cycle gradually decreases from 32.8 to 23.4% with the increase of tensile strain from 3 to 5%. When the remelting beam current was increased to 25 mA and 30 mA, it can be observed in Fig. 9(d) to Fig. 9(i) that the superelastic recovery ratio of the NiTi deposit presented a similar decline with increasing tensile strain. Specifically, the recovery ratio of reversible strain is 23.4%, 21.7%, and 30.4% for remelting beam currents of 20 mA, 25 mA, and 30 mA, respectively, in the first cycle at a loading strain of 5%. Compared to the loading–unloading cycle results of the un-remelted NiTi deposit displayed in Fig. S1(d) and Fig. S1(e) of *Supplementary Materials*, the NiTi deposit prepared with un-remelted condition exhibits a better superelastic recovery, which is mainly attributed to the lower volume fraction of martensite at ambient temperature. However, the elongation of the un-remelted samples did not exceed 5% as detailed in Fig. S1(c) in the *Supplementary Materials* and our previous studies [11]. In addition, the reversible strain stabilizes with the increasing number of loading–unloading cycles, and the stress hysteresis reduces significantly with increasing cyclic strain. The coupled effects of plastic deformation, martensitic phase transformation, and superelastic recovery coexist during cyclic deformation of NiTi SMAs, which all have an inevitable influence on their strain recovery behavior. The specific relationship between plastic deformation and phase transformation will be clarified in detail in *Section 4.3*.

Fig. 10 exhibits the fracture morphologies of the as-deposited NiTi alloys under different remelting beam currents to explore the fracture behavior. The difference in remelting beam currents does not seem to possess a distinct effect on the fracture morphology of NiTi alloys, and obvious tear-ridge and dimples are observed, as shown in Fig. 10(a_1), Fig. 10(b_1), and Fig. 10(c_1). However, the location of microcracks and the distribution of $Ti_4Ni_2O_x$ precipitates are correlated with the tensile properties of as-deposited NiTi alloys by EBF^3-technique. According to the data of Fig. 3, the content of $Ti_4Ni_2O_x$ decreases with the increase of the remelting beam current. Although precipitates can act as stress concentrators and promote the formation of cracks in NiTi deposits, submicron-scale precipitates are also able to prevent or slow down the propagation of microcracks and provide increased ductility to the material [31–33]. As displayed in Fig. 10(a_2), the presence

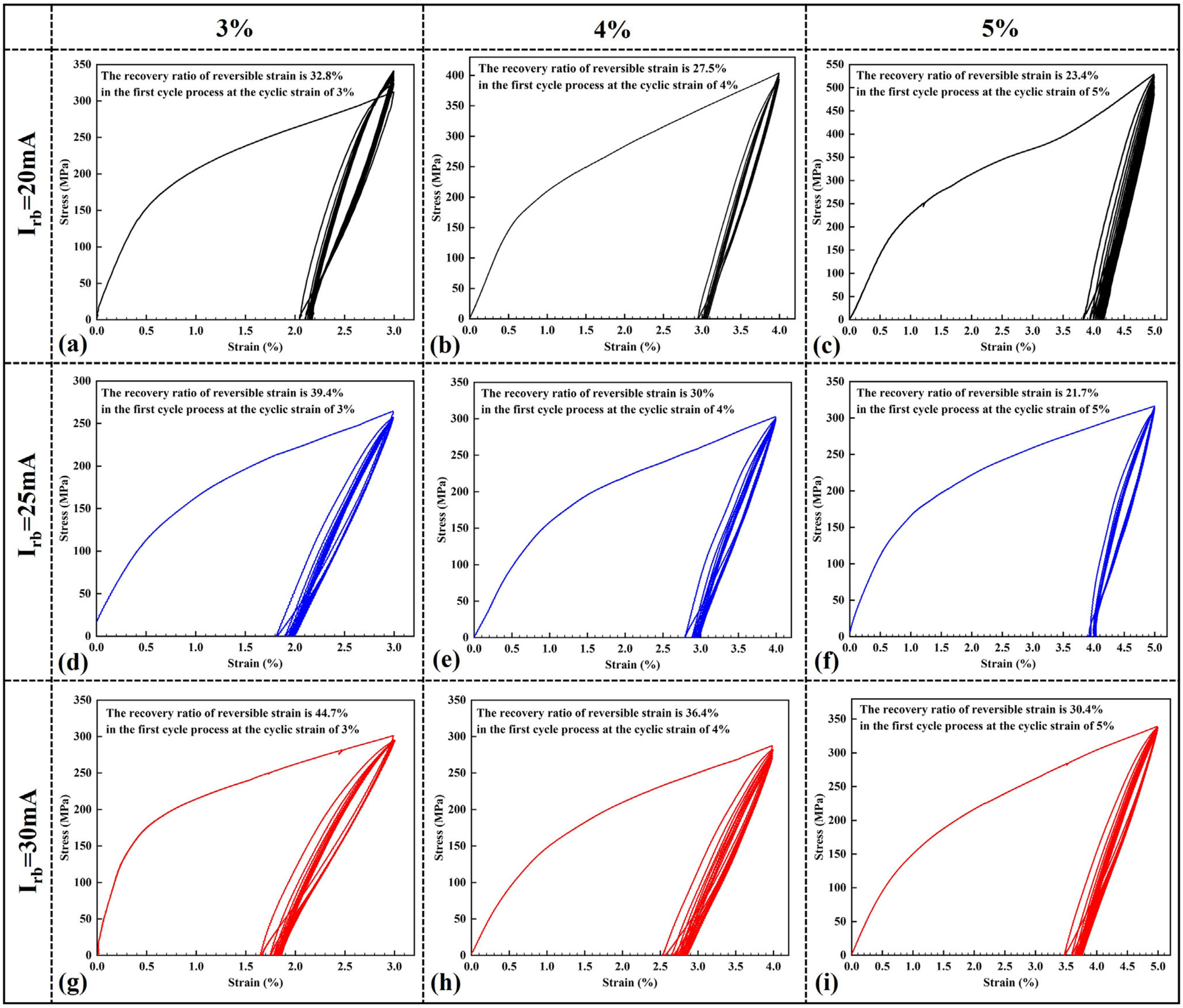

Fig. 9. The loading–unloading cyclic curves at the strain of 3, 4, and 5% for NiTi deposit fabricated under different remelting beam currents: (a), (b), and (c) are 20 mA; (d), (e), and (f) are 25 mA; (g), (h), and (i) are 30 mA.

of $Ti_4Ni_2O_x$ precipitates (solid arrows) in the microcrack (dashed ellipse) aids in inhibiting crack propagation and prevents complete tearing of the NiTi matrix. On the contrary, as can be seen in Fig. 10 (c_2) the microcracks are most probably torn directly from the NiTi matrix. Moreover, submicron-scale precipitates are located in the dimples, as shown in Fig. 10(c_2), which can improve the tensile strength of NiTi alloys. Therefore, the EBF^3-fabricated NiTi deposits illustrated the mechanical performances depicted in Fig. 8 with the increase of remelting beam currents.

4. Discussion

Combined with the results of the *Supplementary Materials* and our previous studies [11,12], the effect of remelting beam currents on the forming quality, chemical composition, precipitates, MTTs, tensile properties, and superelasticity of EBF^3-fabricated NiTi alloys was summarized in Table 3. The relative density and tensile elongation of NiTi alloys were improved after interlayer remelting. A change in the MTT was also observed upon the use of a remelting strategy. In fact, Ni evaporation is positively correlated with the remelting beam currents. Considering the maximum utilization of the superelastic recovery of NiTi alloys, we investigated its superelastic response under different maximum imposed tensile strains. It can be found that the NiTi deposit with a remelting beam current of 20 mA possesses the best elongation to fracture at 6.03% and good superelastic recovery ratio at a strain of 5%. Moreover, we have conducted a general comparison of the overall performance of NiTi alloys prepared by different additive manufacturing techniques, using the samples with a remelting beam current of 20 mA as representative conditions, as listed in Table S1 of the *Supplementary materials*. The results indicated that this NiTi deposit possesses good mechanical and functional properties. Therefore, we analyzed and discussed various aspects, such as microstructure evolution, martensite transformation dependence, plastic deformation, and superelastic response behavior, using specimens fabricated with a remelting beam current of 20 mA as representative condition.

4.1. Correlation of remelting process and microstructure evolution

The microstructure of the as-deposited NiTi alloy in the top layer exhibited the typical solidification microstructure of the mol-

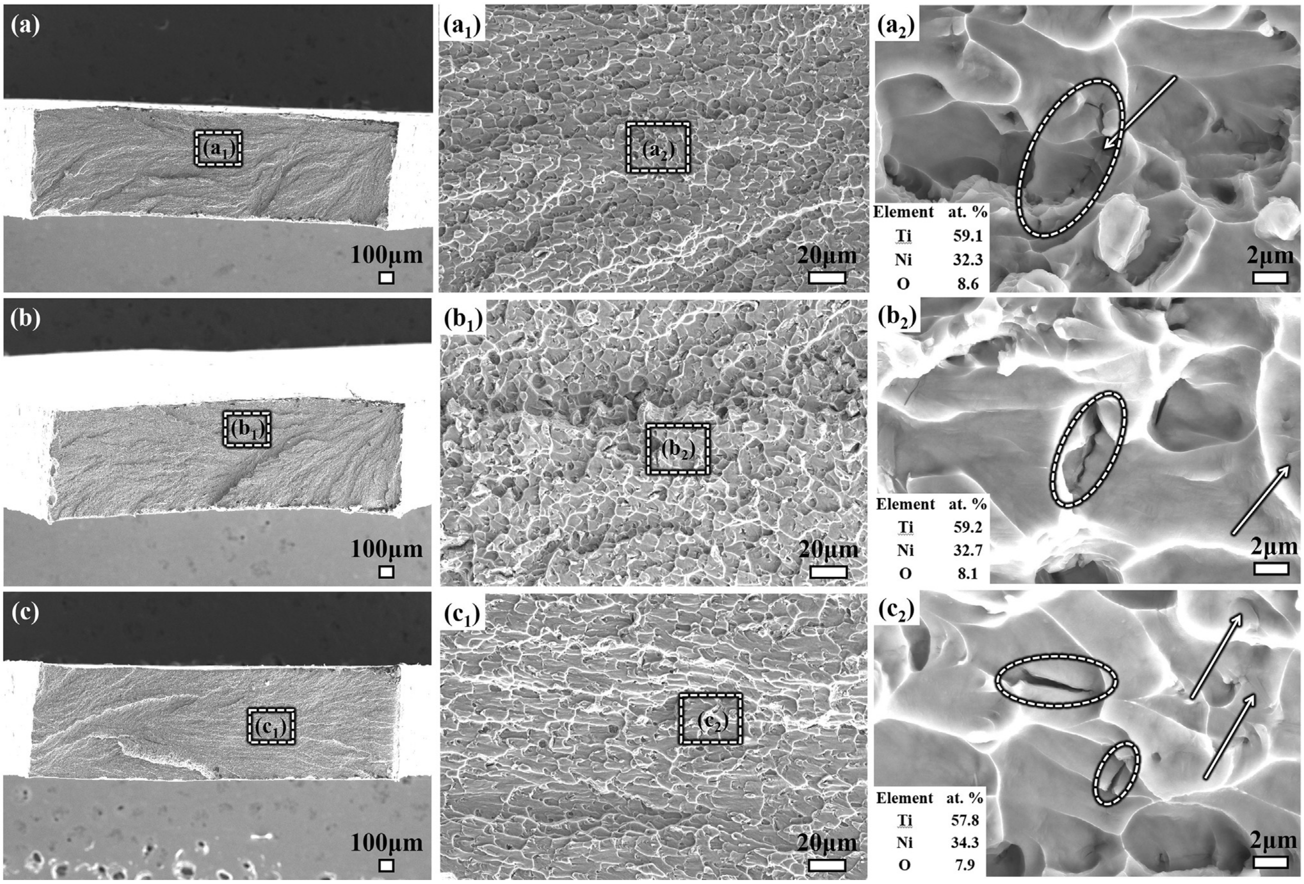

Fig. 10. Fracture morphologies of the as-deposited NiTi alloys under various remelting beam currents: (a), (a_1), and (a_2) are the fracture surfaces from macroscopic to microscopic under a remelting beam current of 20 mA; (b), (b_1), and (b_2) are the fracture surfaces from macroscopic to microscopic with a remelting beam current of 25 mA; (c), (c_1), and (c_2) are the fracture surfaces from macroscopic to microscopic under a remelting beam current of 30 mA. The concentration of different elements in a2, b2, and c2 are the EDS results of the precipitates indicated by the solid arrows.

Table 3
Comparison of EBF^3-fabricated NiTi deposits with and without interlayer remelting.

Samples		Results of un-remelted deposit	Remelting beam currents (mA)		
Aspects			20	25	30
Forming quality	Appearance	Wall structure			
	Relative density (%)	99.6 [12]	99.68	99.79	99.83
Composition of Ni (at. %)	Initial	50.7			
	Deposit	50.4 [12]	50.32	50.28	50.17
Solidification feature	Microstructure	Columnar + equiaxed [11]	Penetrating columnar grains		
	Orientation texture	Cube + Goss [11]	Cube	Cube + Goss	Goss
Precipitates	Type	$Ti_4Ni_2O_x$			
	Volume fraction (%)	1.59 [12]	2.47	1.96	1.56
MTTs (°C)	M_s	−4.6 [12]	1.7	5.6	7.3
	A_f	29.6 [12]	29.8	32.4	34.5
Tensile properties	σ_b (MPa)	578.9 [11]	553.8	563.9	584.1
	ε (%)	4.52 [11]	6.03	5.84	5.77
Tensile superelasticity at strains of 3, 4 and 5%	Recovery ratio (%)	69.8, 69.4, -	32.8, 27.5, 23.4	39.4, 30, 21.7	44.7, 36.4, 30.4

ten pool during fusion-based additive manufacturing of metals, as displayed in Fig. 11(a), i.e. columnar grains and equiaxed grains coexist. During solidification of the molten pool, the large temperature gradient (G) and slow growth rate (R) at the bottom favor the epitaxial growth of columnar grains, while the small G and high R at the top of the melt pool promote the formation of equiaxed grains [34–36]. Similarly, it is clear from Fig. 11(a) that the epitaxially grown columnar grains gradually transform into coarse and irregular polygonal grains or equiaxed grains. Meanwhile, the content of LAGBs in the deposit without interlayer remelting was 0.48, and both Cube {001} ⟨100⟩ texture and Goss {110} ⟨001⟩ texture were present, as shown in Fig. 11(a_1) and Fig. 11(a_2). A beam current of 20 mA was then applied to remelt the surface of its top layer, and the corresponding results are demonstrated in Fig. 11 (b). The microstructure after interlayer remelting is characterized as follows: i) the original coarse and irregular polygonal grains are significantly eliminated; ii) the size of the epitaxially grown columnar grains is also distinctly reduced; iii) a small number of

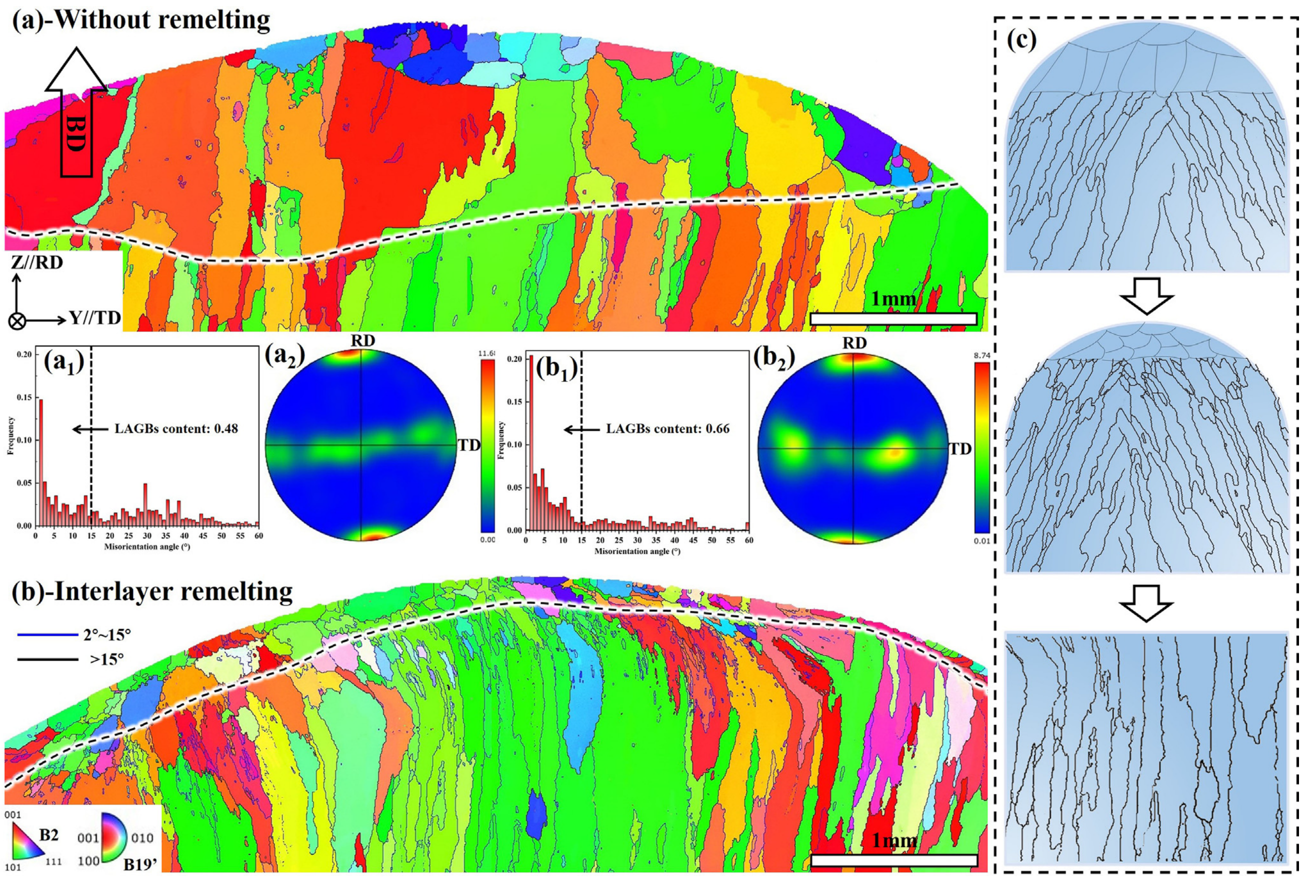

Fig. 11. Effect of remelting on microstructure characteristics of the interlayer: (a) and (b), (a_1) and (b_1), (a_2) and (b_2) are orientation maps and grain boundaries, misorientation, and {100} pole figure of the B2 austenite for the NiTi deposits prepared without interlayer remelting and under a remelting beam current of 20 mA, respectively; (c) schematic of the microstructure formation in the interlayer after the complete remelting process.

equiaxed grains are formed in the top region. This is mainly due to the small remelting beam current between the layers that increases the local temperature gradient and accelerates the cooling rate, which leads to the appearance of the microstructure illustrated in Fig. 11(b). In addition, the content of LAGBs has a concomitant increase to 0.66, and the crystallographic orientation of the B2 austenite phase shifts toward the Goss {110} ⟨001⟩ texture, as exhibited in Fig. 11(b_1) and Fig. 11(b_2). Finally, the residual irregular or equiaxed grains can be completely removed by their own partial remelting when the next layer is deposited again with the processing parameters of beam current, travel speed, and feeding speed set at 45 mA, 600 mm/min, and 3 m/min, respectively. Although various remelting beam currents lead to the differences in microstructural characteristics, as analyzed in Fig. 3, Fig. 5, and Fig. 6, the effect exerted by interlayer remelting is similar. Therefore, after adopting the interlayer remelting strategy in the EBF^3-fabrication process, the NiTi deposit prepared according to the "process-unit" in the current work can be obtained with fully epitaxial columnar grains, whose corresponding microstructure evolution is depicted in Fig. 11(c).

4.2. Dependence of martensitic transformation behavior

It is generally known that the phase transformation of NiTi SMAs is a lattice shear transformation, which is usually dependent on the specific orientation of the austenite phase [24,37–39]. The EBF^3-fabricated NiTi deposit with a remelting beam current of 20 mA consists mainly of the B2 austenite with {001} ⟨100⟩ Cube texture and a small amount of B19′ martensite (1.7 %), as indicated in Fig. 12(a) and Fig. 12(b), which is consistent with the results of Fig. 2. Specifically, the content of martensite in the analyzed region is of 1.7%. Fig. 12(c) and Fig. 12(d) are used to elucidate on the crystallographic orientation of the B19′ martensite located in the boundary of two adjacent austenite grains. It can be confirmed from the corresponding pole figures in Fig. 12(e_2) and Fig. 12(f_3) that the dependence between B2 austenite and B19′ martensite is {110} // {111}. This is mainly attributed to the fact that martensite overcomes and consumes the least amount of energy when starting the shear transformation by propagation or twinning with the closest packed plane of austenite [11,40]. On the other hand, the Rietveld refinement results in Fig. 2 and MTTs listed in Table 2 have proved that the content of martensite increase with the increase of M_s. According to the results of the linear fit in Fig. 12(g) (purple dashed line), the content dependence coefficient (CDC) on M_s is 1.03 %/°C. The well-accepted Clausius-Clapeyron equation has typically a linear correlation between the critical stress (σ^{Ms}) and M_s [41]. Meanwhile, the fitting results of the green dashed line in Fig. 12(g) indicate that the critical stress dependence coefficient (CSDC) on M_s is -3.8 MPa/°C. In other words, the content of martensite is inversely proportional to the σ^{Ms}, i.e., the more residual martensite there is, the easier it is to form stress-induced martensite (SIM) during loading or deformation. This result agrees with the tensile data of Fig. 8. However, the residual martensite, stress induced martensite, superelastic response, and plastic deformation of the as-deposited NiTi alloy under interlayer remelting during the cyclic loading–unloading process encompasses a complex coupling effect. This particular relationship will be discussed in detail in *Section 4.3*.

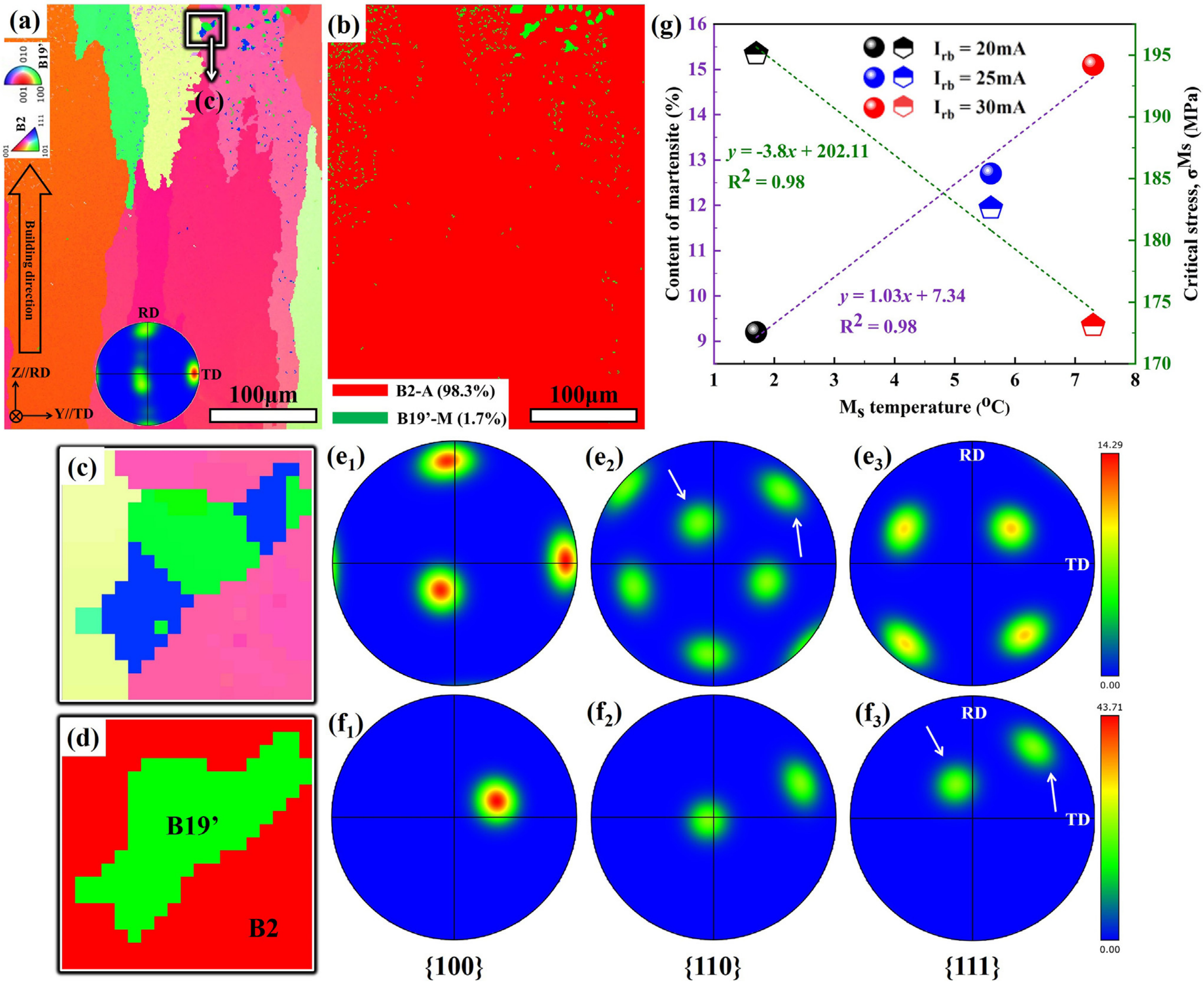

Fig. 12. Dependence of martensitic transformation: (a) and (b) are the orientation maps and phase distribution of EBF^3-fabricated NiTi alloy under a remelting beam current of 20 mA; (c) and (d) are the orientation maps and phase distribution represented by the white rectangular boxes in (a); (e_1), (e_2), and (e_3) are the {1 0 0}, {1 1 0}, and {1 1 1} pole figures of the B2 austenite phase based on the orientation map of (c); (f_1), (f_2), and (f_3) are the {1 0 0}, {1 1 0}, and {1 1 1} pole figures of the B19′ martensite phase based on the orientation map of (c); (g) association of M_s temperature with the content of martensite and critical stress (σ^{Ms}). (The RD and TD marked in e_3 and f_3 are applicable to all pole figures.).

4.3. Relationship between superelastic response and plastic deformation

The cyclic loading–unloading process of NiTi SMAs involves multiple transformation behaviors [42–44]: i) in loading - propagation of residual martensite, stress-induced martensitic transformation, reorientation or detwinning of stress induced martensite, plastic deformation of martensite and austenite; ii) during unloading - the reverse transformation of martensite, dislocation pile-up, martensite stabilization. Meanwhile, the appearance or absence of these microstructure features is tied to the imparted strain during cyclic loading–unloading. As displayed in Fig. 13(a), a small amount of lamellar martensite and dislocation pile-up can be observed when the EBF^3-fabricated NiTi alloy with a remelting beam current of 20 mA is cyclically loaded at a fixed strain of 3%. The SAED pattern and bright-field (BF) image of Fig. 13(a_1) and Fig. 13 (a_2) demonstrates the existence of $Ti_4Ni_2O_x$ precipitates in the B2 austenite matrix, which is in line with the results depicted in Fig. 3 and Fig. 4. Moreover, $Ti_4Ni_2O_x$ precipitates can hinder the propagation or reversion of B19′ martensite and induce a large number of dislocation pile-ups at its front. It can be confirmed in Fig. 13(a_3) to Fig. 13(a_6) that the lamellar martensite belongs to the (0 0 1) compound twin, which is a prevalent twin type in deformed NiTi SMAs [45,46]. After cyclic loading at a strain of 4%, the number and width of residual (0 0 1) compound twins increased significantly, and the dislocation pile-ups in the B2 austenite matrix became more severe, as shown in Fig. 13(b). However, the results in Fig. 13(b_1) and Fig. 13(b_2) illustrate that finer lamellar martensite is present and maintains a specific orientation relationship with the B2 austenite matrix, i.e. $(0\,1\,1)_{B2\ austenite}$ // $(1\,1\,{-1})_{B19'\ martensite}$, which is consistent with the EBSD analysis previously detailed in Fig. 12. Further, as the cyclic loading strain increases to 5%, the original fine lamellar martensite broadens and gradually transforms into a stable structure maintaining the same orientation relationship with the B2 austenite phase, as exhibited in Fig. 13(c), except for the conspicuous precipitates and dislocation pile-ups in the NiTi matrix. Therefore, it can be stated that the broadening and stabilization of lamellar martensite due to dislocation pile-up induced by $Ti_4Ni_2O_x$ precipitates and plastic deformation of austenite and martensite is the essential factor for the decline of superelastic properties in EBF^3-fabricated NiTi alloys.

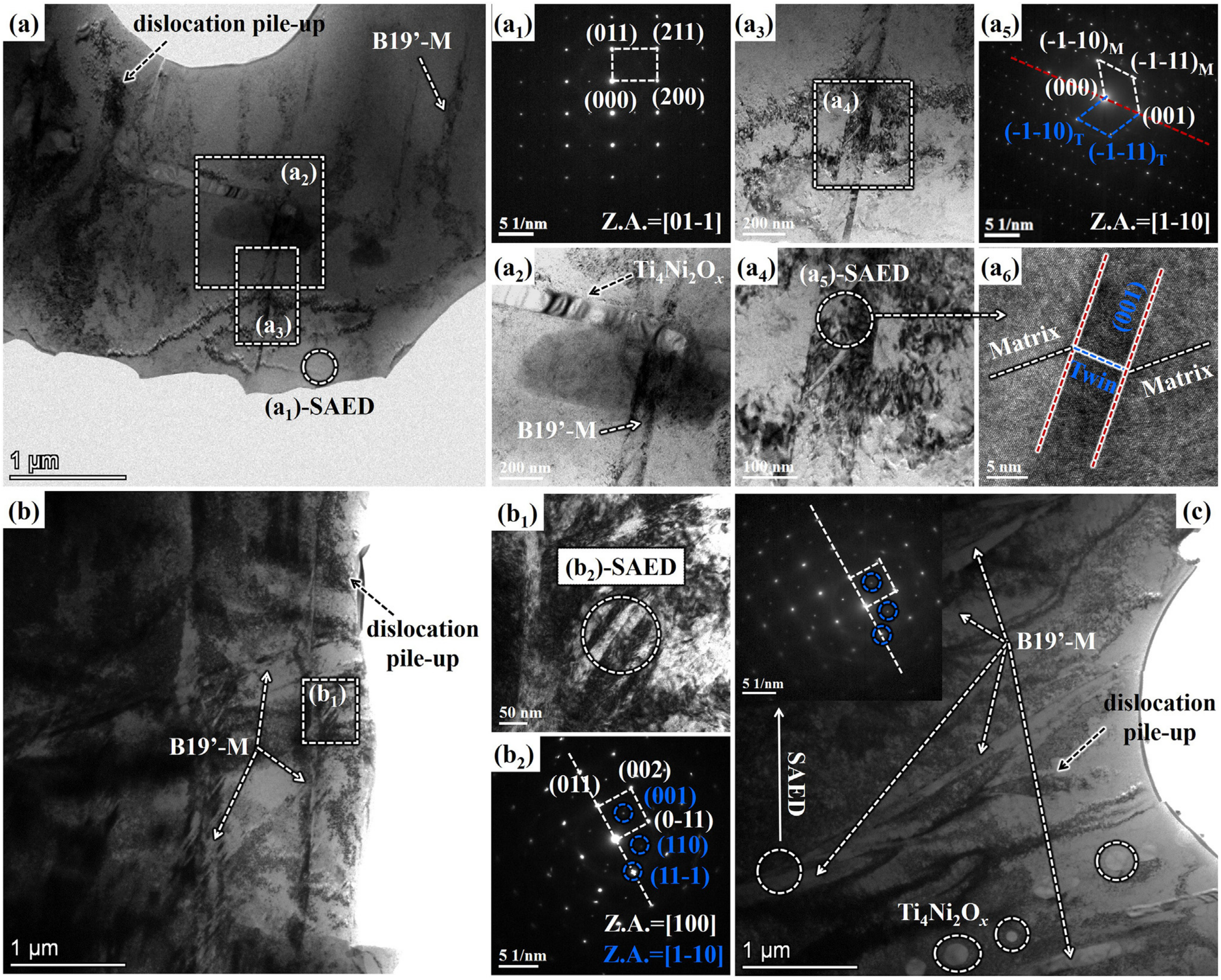

Fig. 13. TEM analysis of the as-deposited NiTi alloy with a remelting beam current of 20 mA after cyclic loading–unloading at various fixed strains: (a) overall bright-field image with a total imposed strain of 3%; (a_1) SAED pattern of the B2 austenite phase; (a_2) hindrance of martensite by precipitates; (a_3) and (a_4) correspond to magnified bright field images of B19′ martensite; (a_5) and (a_6) are the SAED pattern and HRTEM image of (001) compound twins; (b) overall bright-field image with a total imposed strain of 4%; (b_1) and (b_2) are magnified bright-field image and corresponding SAED pattern, where the white and blue represent B2 austenite and B19′ martensite, respectively; (c) overall bright-field image with a total imposed strain of 5% and the SAED pattern of dashed circles.

5. Conclusions and outlooks

Different interlayer remelting strategies were adopted in the current work to investigate its effects on the composition, phase constitution, microstructure evolution, texture characteristics, martensitic transformation, tensile performances, and superelastic behavior of the as-deposited NiTi alloys using EBF^3-technique. The main conclusions are as follows:

(1). The preferential volatilization of Ni in the as-deposited NiTi alloys was intensified with the increase of remelting beam current, which led to a gradual increase in the content of residual martensite at room temperature. However, these alloys are still majorly composed by the B2 austenite, and a small amount of submicron-scale $Ti_4Ni_2O_x$ precipitates formed.

(2). With the increase of remelting beam current, the texture of the B2 austenite phase transformed from {001} ⟨100⟩ into {110} ⟨001⟩ and the content of LAGBs gradually decreased from 0.99 to 0.86. Meanwhile, the selection of an appropriate interlayer remelting strategy can ameliorate the residual strain in the EBF^3-fabricated NiTi deposits, as evidenced by the decrease in average KAM values from 0.58 to 0.42° with increasing remelting beam currents.

(3). A one-step reversible phase transformation between B2 austenite and B19′ martensite was observed in the heating and cooling procedure in the NiTi deposits prepared under different remelting beam currents. The microstructure homogeneity promoted by interlayer remelting keeps the thermal hysteresis, ΔT, of all these NiTi deposits at approximately 27 °C.

(4) The EBF^3-fabricated NiTi deposits with a remelting beam current of 20 mA possessed optimized tensile properties with σ_b and ε of 553.8 MPa and 6.03%, respectively. However, these NiTi alloys have a strong dependence on the martensitic transformation during the tensile procedure, such as the critical stress dependence coefficient on M_s at −3.8 MPa/°C.

(5) Dislocation pile-ups and the residual (001) compound twins gradually increase and broaden with the growth of cyclic loading–unloading strain, and some finer lamellar martensite also appears, which maintains a defined orientation relationship with the

matrix, i.e. (011) $_{B2\ austenite}$ // (11–1) $_{B19'\ martensite}$. Moreover, the $Ti_4Ni_2O_x$ precipitates can restrain the propagation and/or reversion of B19′ martensite. Thus, the broadening and stabilization of martensite result from dislocation pile-ups induced by $Ti_4Ni_2O_x$ precipitates and plastic deformation is the essential reason for the deterioration of the superelastic recovery ratio in EBF^3-fabricated NiTi alloys.

Future research work will focus on: i) simulation of the temperature field and melt flow during the EBF^3-fabrication process supported by numerical calculations to quantitatively illustrate the solidification behavior under different process parameters; ii) directly observe and evaluate the interrelation between martensite transformation and plastic deformation in the deformation process using in-situ characterization to clarify the superelastic response behavior.

CRediT authorship contribution statement

Binqiang Li: Methodology, Investigation, Formal analysis, Data curation, Writing – original draft, Writing – review & editing. **Liang Wang:** Conceptualization, Supervision, Funding acquisition. **Binbin Wang:** Investigation, Funding acquisition, Writing – review & editing. **Donghai Li:** Investigation, Methodology. **J.P. Oliveira:** Funding acquisition, Validation, Formal analysis, Writing – review & editing. **Ran Cui:** Investigation, Formal analysis. **Jianxin Yu:** Investigation, Formal analysis. **Liangshun Luo:** Formal analysis. **Ruirun Chen:** Formal analysis. **Yanqing Su:** Conceptualization, Supervision, Formal analysis. **Jingjie Guo:** Formal analysis. **Hengzhi Fu:** Formal analysis.

Declaration of Competing Interest

The authors declare that they have no known competing financial interests or personal relationships that could have appeared to influence the work reported in this paper.

Acknowledgments

This work was supported by the National Natural Science Foundation of China (Grant no. 51871075, 52171034, and 52101037), Heilongjiang Postdoctoral Fund (Grant no. LBH-Z20139) and the Foundation of National Key Laboratory for Precision Hot Processing of Metals (JCKYS2022603C003). JPO acknowledges Fundação para a Ciência e Tecnologia (FCT - MCTES) for its financial support via the project UID/00667/2020 (UNIDEMI). JPO acknowledges the funding of CENIMAT/i3N by national funds through the FCT-Fundação para a Ciência e a Tecnologia, I.P., within the scope of Multiannual Financing of R&D Units, reference UIDB/50025/2020-2023.

Data Availability

The data that support the findings of this research are available from the corresponding author, specifically Professor Yanqing Su of the Harbin Institute of Technology (email: suyq@hit.edu.cn) upon reasonable request.

Appendix A. Supplementary material

Supplementary data to this article can be found online at https://doi.org/10.1016/j.matdes.2022.110886.

References

[1] J.P. Oliveira, R.M. Miranda, F.M. Braz Fernandes, Welding and joining of NiTi shape memory alloys: a review, Prog. Mater. Sci. 88 (2017) 412–466, https://doi.org/10.1016/j.pmatsci.2017.04.008.
[2] Q. Zhang, S. Hao, Y. Liu, Z. Xiong, W. Guo, Y. Yang, Y. Ren, L. Cui, L. Ren, Z. Zhang, The microstructure of a selective laser melting (SLM)-fabricated NiTi shape memory alloy with superior tensile property and shape memory recoverability, Appl. Mater. Today 19 (2020), https://doi.org/10.1016/j.apmt.2019.100547 100547.
[3] M. Elahinia, N. Shayesteh Moghaddam, M. Taheri Andani, A. Amerinatanzi, B.A. Bimber, R.F. Hamilton, Fabrication of NiTi through additive manufacturing: a review, Prog. Mater. Sci. 83 (2016) 630–663, https://doi.org/10.1016/j.pmatsci.2016.08.001.
[4] I.D. McCue, G.M. Valentino, D.B. Trigg, A.M. Lennon, C.E. Hebert, D.P. Seker, S.M. Nimer, J.P. Mastandrea, M.M. Trexler, S.M. Storck, Controlled shape-morphing metallic components for deployable structures, Mater. Des. 208 (2021), https://doi.org/10.1016/j.matdes.2021.109935 109935.
[5] R.F. Hamilton, B.A. Bimber, M. Taheri Andani, M. Elahinia, Multi-scale shape memory effect recovery in NiTi alloys additive manufactured by selective laser melting and laser directed energy deposition, J. Mater. Process. Tech. 250 (2017) 55-64, http://dx.doi.org/10.1016/j.jmatprotec.2017.06.027.
[6] D. Svetlizky, M. Das, B. Zheng, A.L. Vyatskikh, S. Bose, A. Bandyopadhyay, J.M. Schoenung, E.J. Lavernia, N. Eliaz, Directed energy deposition (DED) additive manufacturing: physical characteristics, defects, challenges and applications, Mater. Today 49 (2021) 271–295, https://doi.org/10.1016/j.mattod.2021.03.020.
[7] J. Dutkiewicz, Ł. Rogal, D. Kalita, M. Węglowski, S. Błacha, K. Berent, T. Czeppe, A. Antolak-Dudka, T. Durejko, T. Czujko, Superelastic effect in NiTi alloys manufactured using electron beam and focused laser rapid manufacturing methods, J. Mater. Eng. Perform. 29 (2020) 4463–4473, https://doi.org/10.1007/s11665-020-04938-z.
[8] RPM Guimarães, F. Pixner, G. Trimmel, J. Hobisch, T. Rath, F. Fernandez, N. Enzinger, S.T. Amancio-Filho, The electron beam freeform fabrication of NiTi shape memory alloys. part I: microstructure and physical-chemical behavior, Proc. Inst. Mech. Eng. Pt. L-J. Mater. -Des. Appl. 235 (4) (2021) 709–716.
[9] Z. Pu, D. Du, K. Wang, G. Liu, D. Zhang, X. Wang, B. Chang, Microstructure, phase transformation behavior and tensile superelasticity of NiTi shape memory alloys fabricated by the wire-based vacuum additive manufacturing, Mater. Sci. Eng. A 812 (2021), https://doi.org/10.1016/j.msea.2021.141077 141077.
[10] J. Dutkiewicz, Ł. Rogal, D. Kalita, J. Kawałko, M.S. Węglowski, K. Kwieciński, P. Śliwiński, H. Danielewski, B. Antoszewski, E. Cesari, Microstructure, mechanical properties, and martensitic transformation in NiTi shape memory alloy fabricated using electron beam additive manufacturing technique, J. Mater. Eng. Perform. 31 (2022) 1609–1621, https://doi.org/10.1007/s11665-021-06241-x.
[11] B. Li, L. Wang, B. Wang, D. Li, R. Cui, B. Su, L. Yao, L. Luo, R. Chen, Y. Su, J. Guo, H. Fu, Solidification characterization and its correlation with the mechanical properties and functional response of NiTi shape memory alloy manufactured by electron beam freeform fabrication, Addi. Manuf. 48 (2021), https://doi.org/10.1016/j.addma.2021.102468 102468.
[12] B. Li, L. Wang, B. Wang, D. Li, J.P. Oliveira, R. Cui, J. Yu, L. Luo, R. Chen, Y. Su, J. Guo, H. Fu, Electron beam freeform fabrication of niti shape memory alloys: crystallography, martensitic transformation, and functional response, Mater. Sci. Eng. A 843 (2022), https://doi.org/10.1016/j.msea.2022.143135 143135.
[13] L.E. Dos Santos Paes, M. Pereira, F.A. Xavier, W.L. Weingaertner, L.O. Vilarinho, Lack of fusion mitigation in directed energy deposition with laser (DED-L) additive manufacturing through laser remelting, J. Manuf. Process. 73 (2022) 67–77, https://doi.org/10.1016/j.jmapro.2021.10.052.
[14] J. Wang, Y. Lu, F. Jia, W. Xia, F. Lin, J. Han, R. Wang, Z. Pan, H. Li, Z. Jiang, Effects of inter-layer remelting frequency on the microstructure evolution and mechanical properties of equimolar CoCrFeNiMn high entropy alloys during in-situ powder-bed arc additive manufacturing (PBAAM) process, J. Mater. Sci. Technol. 113 (2022) 90–104, https://doi.org/10.1016/j.jmst.2021.10.001.
[15] T. Gustmann, H. Schwab, U. Kühn, S. Pauly, Selective laser remelting of an additively manufactured Cu-Al-Ni-Mn shape-memory alloy, Mater. Des. 153 (2018) 129–138, https://doi.org/10.1016/j.matdes.2018.05.010.
[16] J. Zhan, Y. Lu, J. Lin, On the martensitic transformation temperatures and mechanical properties of NiTi alloy manufactured by selective laser melting: effect of remelting, Acta Metall. Sin. 34 (2021) 1223–1233, https://doi.org/10.1007/s40195-021-01212-6.
[17] S. Gao, O.P. Bodunde, M. Qin, W. Liao, P. Guo, Microstructure and phase transformation of nickel-titanium shape memory alloy fabricated by directed energy deposition with in-situ heat treatment, J. Alloy. Compd. 898 (2022), https://doi.org/10.1016/j.jallcom.2021.162896 162896.
[18] X. Wang, J. Yu, J. Liu, L. Chen, Q. Yang, H. Wei, J. Sun, Z. Wang, Z. Zhang, G. Zhao, J. Van Humbeeck, Effect of process parameters on the phase transformation behavior and tensile properties of NiTi shape memory alloys fabricated by selective laser melting, Addi. Manuf 36 (2020), https://doi.org/10.1016/j.addma.2020.101545 101545.
[19] R.F. Hamilton, B.A. Bimber, T.A. Palmer, Correlating microstructure and superelasticity of directed energy deposition additive manufactured Ni-rich NiTi alloys, J. Alloy. Compd. 739 (2018) 712–722, https://doi.org/10.1016/j.jallcom.2017.12.270.
[20] Q. Zhou, M.D. Hayat, G. Chen, S. Cai, X. Qu, H. Tang, P. Cao, Selective electron beam melting of NiTi: microstructure, phase transformation and mechanical properties, Mater. Sci. Eng. A 744 (2019) 290–298, https://doi.org/10.1016/j.msea.2018.12.023.
[21] D. Li, H. Huang, C. Chen, S. Liu, X. Liu, X. Zhang, K. Zhou, Additive manufacturing of high strength near β titanium alloy Ti-55511 by

engineering nanoscale secondary α laths via in-situ heat treatment, Mater. Sci. Eng. A 814 (2021), https://doi.org/10.1016/j.msea.2021.141245 141245.
[22] Y. Li, S. Wu, H. Li, Y. Dong, F. Cheng, Submerged arc additive manufacturing (SAAM) of low-carbon steel: Effect of in-situ intrinsic heat treatment (IHT) on microstructure and mechanical properties, Addi. Manuf 46 (2021), https://doi.org/10.1016/j.addma.2021.102124 102124.
[23] W.J. Sames, K.A. Unocic, G.W. Helmreich, M.M. Kirka, F. Medina, R.R. Dehoff, S. S. Babu, Feasibility of in situ controlled heat treatment (ISHT) of Inconel 718 during electron beam melting additive manufacturing, Addi. Manuf 13 (2017) 156–165, https://doi.org/10.1016/j.addma.2016.09.001.
[24] K. Otsuka, X. Ren, Physical metallurgy of Ti-Ni-based shape memory alloys, Prog. Mater. Sci. 50 (2005) 511–678, https://doi.org/10.1016/j.pmatsci.2004.10.001.
[25] J. Frenzel, A. Wieczorek, I. Opahle, B. Maaß, R. Drautz, G. Eggeler, On the effect of alloy composition on martensite start temperatures and latent heats in Ni-Ti-based shape memory alloys, Acta Mater. 90 (2015) 213–231, https://doi.org/10.1016/j.actamat.2015.02.029.
[26] B. Feng, C. Wang, Q. Zhang, Y. Ren, L. Cui, Q. Yang, S. Hao, Effect of laser hatch spacing on the pore defects, phase transformation and properties of selective laser melting fabricated NiTi shape memory alloys, Mater. Sci. Eng. A 840 (2022), https://doi.org/10.1016/j.msea.2022.142965 142965.
[27] W. Guo, B. Feng, Y. Yang, Y. Ren, Y. Liu, H. Yang, Q. Yang, L. Cui, X. Tong, S. Hao, Effect of laser scanning speed on the microstructure, phase transformation and mechanical property of NiTi alloys fabricated by LPBF, Mater. Des. 215 (2022), https://doi.org/10.1016/j.matdes.2022.110460 110460.
[28] G.S. Firstov, T.A. Kosorukova, Y.N. Koval, P.A. Verhovlyuk, Directions for high-temperature shape memory alloys' improvement: straight way to high-entropy materials?, Shap Mem. Superelasticity 1 (2015) 400–407, https://doi.org/10.1007/s40830-015-0039-7.
[29] P. Nnamchi, A. Younes, S. González, A review on shape memory metallic alloys and their critical stress for twinning, Intermetallics 105 (2019) 61–78, https://doi.org/10.1016/j.intermet.2018.11.005.
[30] P. Chowdhury, H. Sehitoglu, Deformation physics of shape memory alloys-fundamentals at atomistic frontier, Prog. Mater. Sci. 88 (2017) 49–88, https://doi.org/10.1016/j.pmatsci.2017.03.003.
[31] H.Z. Lu, C. Yang, X. Luo, H.W. Ma, B. Song, Y.Y. Li, L.C. Zhang, Ultrahigh-performance TiNi shape memory alloy by 4D printing, Mater. Sci. Eng. A 763 (2019), https://doi.org/10.1016/j.msea.2019.138166 138166.
[32] H.Z. Lu, L.H. Liu, C. Yang, X. Luo, C.H. Song, Z. Wang, J. Wang, Y.D. Su, Y.F. Ding, L.C. Zhang, Y.Y. Li, Simultaneous enhancement of mechanical and shape memory properties by heat-treatment homogenization of Ti_2Ni precipitates in TiNi shape memory alloy fabricated by selective laser melting, J. Mater. Sci. Technol. 101 (2022) 205–216, https://doi.org/10.1016/j.jmst.2021.06.019.
[33] B. Lu, X. Cui, W. Ma, M. Dong, Y. Fang, X. Wen, G. Jin, D. Zeng, Promoting the heterogeneous nucleation and the functional properties of directed energy deposited NiTi alloy by addition of La_2O_3, Addi. Manuf. 33 (2020), https://doi.org/10.1016/j.addma.2020.101150 101150.
[34] H.L. Wei, T. Mukherjee, W. Zhang, J.S. Zuback, G.L. Knapp, A. De, T. DebRoy, Mechanistic models for additive manufacturing of metallic components, Prog. Mater. Sci. 116 (2021), https://doi.org/10.1016/j.pmatsci.2020.100703 100703.
[35] C. Körner, M. Markl, J.A. Koepf, Modeling and simulation of microstructure evolution for additive manufacturing of metals: A critical review, Metall. Mater. Trans. A-Phys. Metall, Mater. Sci. 51 (2020) 4970–4983, https://doi.org/10.1007/s11661-020-05946-3.
[36] T. Wang, Y.Y. Zhu, S.Q. Zhang, H.B. Tang, H.M. Wang, Grain morphology evolution behavior of titanium alloy components during laser melting deposition additive manufacturing, J. Alloy. Compd. 632 (2015) 505–513, https://doi.org/10.1016/j.jallcom.2015.01.256.
[37] A.P. Stebner, H.M. Paranjape, B. Clausen, L.C. Brinson, A.R. Pelton, In situ neutron diffraction studies of large monotonic deformations of superelastic Nitinol, Shap. Mem. Superelasticity 1 (2015) 252–267, https://doi.org/10.1007/s40830-015-0015-2.
[38] W.S. Choi, E.L. Pang, W. Ko, H. Jun, H.J. Bong, C. Kirchlechner, D. Raabe, P. Choi, Orientation-dependent plastic deformation mechanisms and competition with stress-induced phase transformation in microscale NiTi, Acta Mater. 208 (2021), https://doi.org/10.1016/j.actamat.2021.116731 116731.
[39] G. Ma, S. Qin, J. Shang, F. Wang, Y. Chen, Atomistic study on the phase transformation in NiTi under thermal cycling, J. Alloy. Compd. 705 (2017) 218–225, https://doi.org/10.1016/j.jallcom.2017.02.094.
[40] M. Wang, S. Jiang, D. Sun, Y. Zhang, Orientation dependence of mechanical behavior and phase transformation of NiTi shape memory alloy with multilayer structures by molecular dynamics simulation, J. Mater. Res. Technol-JMRT 18 (2022) 943–961, https://doi.org/10.1016/j.jmrt.2022.02.125.
[41] Y. Yang, J.B. Zhan, B. Li, J.X. Lin, J.J. Gao, Z.Q. Zhang, L. Ren, P. Castany, T. Gloriant, Laser beam energy dependence of martensitic transformation in SLM fabricated NiTi shape memory alloy, Materialia 6 (2019), https://doi.org/10.1016/j.mtla.2019.100305 100305.
[42] X. Bian, L. Heller, L. Kadeřávek, P. Šittner, In-situ synchrotron X-ray diffraction texture analysis of tensile deformation of nanocrystalline NiTi wire in martensite state, Appl. Mater. Today 26 (2022), https://doi.org/10.1016/j.apmt.2022.101378 101378.
[43] O. Molnárová, O. Tyc, L. Heller, H. Seiner, P. Šittner, Evolution of martensitic microstructures in nanocrystalline NiTi wires deformed in tension, Acta Mater. 218 (2021), https://doi.org/10.1016/j.actamat.2021.117166 117166.
[44] J.P. Oliveira, F.M.B. Fernandes, N. Schell, R.M. Miranda, Martensite stabilization during superelastic cycling of laser welded NiTi plates, Mater. Lett. 171 (2016) 273–276, https://doi.org/10.1016/j.matlet.2016.02.107.
[45] J. Pfetzing-Micklich, R. Ghisleni, T. Simon, C. Somsen, J. Michler, G. Eggeler, Orientation dependence of stress-induced phase transformation and dislocation plasticity in NiTi shape memory alloys on the micro scale, Mater. Sci. Eng. A 538 (2012) 265–271, https://doi.org/10.1016/j.msea.2012.01.042.
[46] S.C. Mao, J.F. Luo, Z. Zhang, M.H. Wu, Y. Liu, X.D. Han, EBSD studies of the stress-induced B2-B19′ martensitic transformation in NiTi tubes under uniaxial tension and compression, Acta Mater. 58 (2010) 3357-3366, https://doi.org/10.1016/j.actamat.2010.02.009.